Ultramicroscopy 182 (2017) 44–53

Contents lists available at ScienceDirect

Ultramicroscopy

journal homepage: www.elsevier.com/locate/ultramic

Characterisation of the Medipix3 detector for 60 and 80 keV electrons

J.A. Mir[a], R. Clough[a], R. MacInnes[c], C. Gough[c], R. Plackett[b], I. Shipsey[b], H. Sawada[a,e,f], I. MacLaren[c], R. Ballabriga[d], D. Maneuski[c], V. O'Shea[c], D. McGrouther[c,*], A.I. Kirkland[a,e]

[a] University of Oxford, Department of Materials, Parks Road, Oxford OX1 3PH, United Kingdom
[b] University of Oxford, Department of Physics, Parks Road, Oxford OX1 3PH, United Kingdom
[c] University of Glasgow, School of Physics and Astronomy, Glasgow G12 8QQ, United Kingdom
[d] CERN, 1211 Geneva 23, Geneva, Switzerland
[e] Electron Physical Sciences Imaging Centre, Diamond Light Source Ltd, Harwell Science & Innovation Campus, Didcot, Oxfordshire OX11 0DE, United Kingdom
[f] JEOL UK Ltd. JEOL House, Silvercourt, Watchmead, Welwyn garden City, Herts AL71LT, United Kingdom

ARTICLE INFO

Article history:
Received 20 December 2016
Revised 4 May 2017
Accepted 12 June 2017
Available online 20 June 2017

Keywords:
Medipix3
Single pixel mode
Charge summing mode
TEM, MTF
DQE
Nyquist frequency

ABSTRACT

In this paper we report quantitative measurements of the imaging performance for the current generation of hybrid pixel detector, Medipix3, used as a direct electron detector. We have measured the modulation transfer function and detective quantum efficiency at beam energies of 60 and 80 keV. In single pixel mode, energy threshold values can be chosen to maximize either the modulation transfer function or the detective quantum efficiency, obtaining values near to, or exceeding those for a theoretical detector with square pixels. The Medipix3 charge summing mode delivers simultaneous, high values of both modulation transfer function and detective quantum efficiency. We have also characterized the detector response to single electron events and describe an empirical model that predicts the detector modulation transfer function and detective quantum efficiency based on energy threshold. Exemplifying our findings we demonstrate the Medipix3 imaging performance recording a fully exposed electron diffraction pattern at 24-bit depth together with images in single pixel and charge summing modes. Our findings highlight that for transmission electron microscopy performed at low energies (energies <100 keV) thick hybrid pixel detectors provide an advantageous architecture for direct electron imaging.

1. Introduction

Direct electron detection can be achieved using the conventional film or various solid-state detection architectures including monolithic active pixel sensors (MAPS) [1] or variants of hybrid pixel detector technology [2,3] such as the Medipix3 sensors. MAPS technology forms the basis of many current direct detector systems that are widely applied for cryogenic transmission electron microscopy imaging in life sciences [4] and are beginning to be used in selected materials science applications [5]. This family of detectors typically feature pixels with 6–10 μm lateral size, containing several transistors per pixel and with array sizes greater than 1 megapixel. Silicon wafer thinning processes have been developed such that the entire detector thickness can be reduced to around ca. 25 μm [1,4]. For this class of detectors primary electrons at energies, >200 keV, are mostly transmitted through the sensor depositing only a fraction of their energy with lateral spread within 1–2 pixels. Counting of single electron events can be achieved using off-chip image processing hardware to process multiple short exposure frames [4]. However, for MAPS detectors operated at lower primary electron energies imaging performance is compromised due to increased scattering leading to signal across many pixels. Primary energies lower than 100 keV can provide greater contrast for thin biological samples [6] or the avoidance of knock-on damage, for example in imaging 2-dimensional materials containing light elements [7]. For these applications, the alternative architecture of hybrid pixel detectors may offer advantages.

In contrast to MAPS, hybrid pixel detectors consist of a relatively thick, (hundreds of μm), sensitive semiconductor layer connected to a separate but immediately adjacent readout ASIC that processes the signal in the sensor. In this study, we demonstrate, using the Medipix3 sensor that a thick silicon hybrid with coarse pixel geometry is ideal for low voltage Transmission Electron Microscopy (TEM) imaging up to 80 keV where the Modulation Transfer Function (MTF) is almost invariant and yields high Detective Quantum Efficiencies (DQE).

* Corresponding author.
E-mail address: damien.mcgrouther@glasgow.ac.uk (D. McGrouther).

http://dx.doi.org/10.1016/j.ultramic.2017.06.010
0304-3991/

2. Background: detector operation

The Medipix3 detector was designed at CERN within the framework of the Medipix3 collaboration for photon and particle detection and fabricated using commercial 0.13 µm CMOS technology. The sensitive matrix consists of 256×256 pixels at 55 µm pitch with an overall area of 15.88×14.1 mm^2. The readout chip is connected to a 300 µm thick silicon layer. Each pixel contains analogue circuitry consisting of a charge sensitive preamplifier (CSA), and a semi-Gaussian shaper which produces a voltage pulse proportional to the electron (or hole) current collected at the pixel bump bond. The voltage pulse is compared to two discriminators that control the lower and upper threshold levels. Each discriminator has a 5-bit digital to analogue converter (DAC) whose values are adjusted during initial equalization to reduce the threshold dispersion caused by any mismatch in the pixel transistors. When operating in single pixel mode (SPM), if the deposited energy exceeds the preset lower threshold energy value, TH0, then a count is registered in the digital pixel circuitry. Energy calibration of the thresholds is performed using flat-field illumination of the detector with an X-ray source providing a range of photon energies [2]. Each pixel contains two configurable depth registers (2×12-bit) which can also function to enable a continuous read–write capability in which one register acts as a counter whilst the other shifts the data for readout. Alternatively, the two counters can be linked to provide 24-bit depth counting.

When compared to the earlier Medipix2 detector [8,9], the Medipix3 design contains additional analogue and digital circuitry for the implementation of a charge summing mode (CSM). This is designed to mitigate the effects of charge sharing. Charge sharing occurs when either the primary radiation (incident beam electrons in this case) undergoes lateral dispersion as they lose energy in the silicon slab or when the resulting secondary electron (hole) charge cloud is broadened by diffusion. Both processes spread charge across several pixels leading to degradation in both energy and spatial resolution. For incident electrons, in contrast to X-ray photons, the primary effect is most significant, whereby the electrons lose energy sporadically through inelastic scattering events distributed over tens of micrometres (for beam energies of the order of tens of keV). The CSM implemented in the Medipix3 detector has been designed to minimize the effect of charge sharing by summing charge deposited in clusters of immediate neighbouring pixels at pixel corners and allocating the reconstructed charge to the pixel with the highest collected charge. This is accomplished in several steps. As an example, if charge created from the initial electron event encompasses four pixels then the individual pixel charges are compared to TH0. The digital circuitry within the pixels processes the charge distribution to identify the pixel with the largest charge and inhibits the pixels with lower signal. In parallel the charge is reconstructed in analogue summing circuits located at the corners of each pixel and compared to a second energy threshold, TH1. The pixel with the highest local charge increases its counter if the reconstructed charge in at least one of its adjacent summing nodes is above TH1 [10,11].

We have used a single chip Medipix3 detector to investigate its performance for TEM applications at 60 and 80 keV. The basic metrics used for quantifying the detector performance are the MTF and the DQE. The MTF is defined as the ratio of output to input modulation as a function of spatial frequency and effectively describes how the detection system attenuates the amplitudes of an infinite sinusoidal series. In the present work, we used the established knife edge method [12,13] to derive the MTF as well as a new alternative technique to calculate the point spread function (PSF) directly from short exposure flat-field images capturing single electron events.

For the knife-edge method, a line spread function (LSF) was initially obtained by differentiating an experimentally obtained edge profile. The modulus of the Fourier transform of the LSF yields the MTF. The DQE is defined as the ratio of square of the output to the square of the input signal-to-noise (SNR):

$$\mathrm{DQE}(f) = \frac{[\mathrm{SNR}_{\mathrm{out}}(f)]^2}{[\mathrm{SNR}_{\mathrm{in}}(f)]^2} \tag{1}$$

where f is the spatial frequency. As previously reported the DQE can be conveniently calculated from the MTF and the noise power spectrum (NPS) as [9,13]:

$$\mathrm{DQE}(f) = \frac{c^2 \mathrm{MTF}^2}{n(\mathrm{NPS})} \tag{2}$$

in which, c, represents the number of counts in the output image and n is the input electron dose and where NPS describes spatial frequency dependence of the noise [13]. Hence, in order to calculate the DQE, experimental measurements of the MTF, NPS and the gain factor, g, defined as the ratio c/n for a given operational voltage are required.

The NPS was calculated from the Fourier transform of flatfield images recorded under uniform illumination. The MTF and the DQE were evaluated in the spatial frequency range from 0 to 0.5 pixel^{-1} where the upper limit represents the Nyquist frequency beyond which aliasing occurs. In the present case, this limit corresponds to 9.1 lp/mm. As described previously [9,13], it is difficult to calculate the NPS and hence the DQE at lower spatial frequencies accurately. The observed variance in a flat-field image results in underestimation of the true noise per pixel as the charge produced by an incident electron is seldom confined to a single pixel. We have carried out a similar analysis to [9] using Eq. (1) to calculate the DQE at zero spatial frequency, DQE (0), detailed subsequently in Section 2.

The MTF of the detector arises from the manner in which electrons deposit their energy in the sensitive silicon sensor layer and by which the resultant electron–hole pairs diffuse under bias toward the readout ASIC circuitry. Given that the energy required to produce a single electron–hole pair is 3.6 eV in silicon, a single primary electron at 60 keV can produce over 16,000 electron–hole pairs. However due to the high SNR of the Medipix3 sensor we have been able to perform analysis of single electron events during short shutter exposures, with durations in the range 1–10 µs, that show both single and multi-pixel clusters. Characterisation of cluster area and detector response was carried out as a function of threshold energy and synthetic PSFs calculated from which MTFs were subsequently calculated by Fourier transformation of the PSF.

3. Experimental

The Medipix3 detector was mounted on the JEOL ARM200CF TEM/STEM [14] in a custom mount interfaced to the 35 mm camera port located above the viewing screen. This mount included a vacuum feed through for a 68 way electrical connector for the necessary readout electronics. Operation and high speed data readout of the detector used MERLIN hardware/software produced by quantum detectors [15]. MTF and DQE data was recorded for primary electron beam energies of 60 and 80 keV using both SPM and CSM modes. For each primary electron energy, the MTF data was recorded from images of a 2 mm thick Al knife edge inclined by 10° with respect to the pixel readout columns. For an exposure time of 10 ms, 32 images were acquired across the full range of Medipix3 energy threshold values in the SPM mode. The MTF data acquisition procedure was then repeated in the CSM mode by holding TH0 at a fixed energy and scanning the high threshold (TH1) DAC across the full range of energy values.

For primary electron energies of 60 and 80 keV, a set of 32 flatfield images were acquired as a function of threshold energy val-

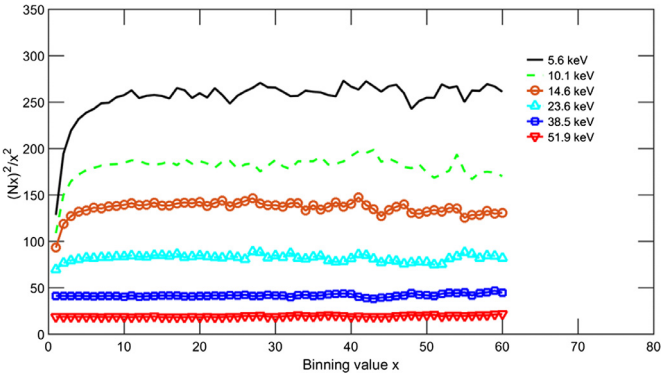

Fig. 1. Variation in noise, $(N_x)^2/x^2$ as a function of x-fold binning at 60 keV for various TH0 thresholds.

ues and used to calculate the NPS, and subsequently the DQE using Eq. (2). This was accomplished with 10 ms exposure times using SPM and CSM modes. Calibration of the required energy thresholds was performed taking into account certain criteria. For both SPM and CSM modes, when the energy threshold is equal to the incident beam energy, the total integrated counts must reduce to zero. In addition, for the SPM mode, additional calibration points were measured by identifying the threshold DAC values where electron impacts resulted in only single pixel hits, i.e. at the half of the incident beam energy [9]. The gain factors, g, for the specified primary electron energies were measured by imaging the full electron beam diameter within the detector perimeter and recording 32 images [13] for a range of threshold energy values. For each primary beam energy, the beam current was measured by focusing the beam within the small viewing screen and measuring the current with a Keithley 485 Pico ammeter. The following equation summarises the dependence of g on the measured current, exposure time and the pixel sum values:

$$g = \frac{\text{Current} \times \text{Exposure time}}{\text{Pixel sum} \times e} \tag{3}$$

4. Determination of the MTF and DQE

DQE(0) was measured using the method described previously [9,13,16] where the noise $(N_x)^2$ is measured in x by x binned images with increasing x. In this work, 32 flat-field images were analysed where each subsequent image had the previous image in the series subtracted to produce 31 images of uniform illumination with a mean pixel value. The noise per pixel was found from locating the plateau in $(N_x)^2/x^2$ as a function of x. Fig. 1 shows a typical noise evaluation used to calculate DQE(0) using 60 keV flat-field SPM images for different threshold DAC values. As expected the noise per pixel reduces with increasing threshold DAC values, as the variance reduces with decreasing effective pixel size. After extracting the noise per pixel values at the plateau in $(N_x)^2/x^2$, DQE(0) for a given DAC value was calculated using Eq. (4):

$$\text{DQE}(0) = \frac{c^2}{0.5\left(\frac{N_x^2}{x^2}\right)/n} \tag{4}$$

Fig. 2 shows the variation of MTF as a function of spatial frequency at 60 and 80 keV using SPM for various TH0 energy thresholds. At the highest value of TH0 the MTF in single pixel mode is better than the theoretical maximum due to the reduction in the effective pixel size [8]. However, the DQE at high TH0 values in SPM is significantly reduced as shown in Figs. 3 and 4. This is a consequence of many electron events not being counted because, for these, the charge is deposited in more than one pixel and

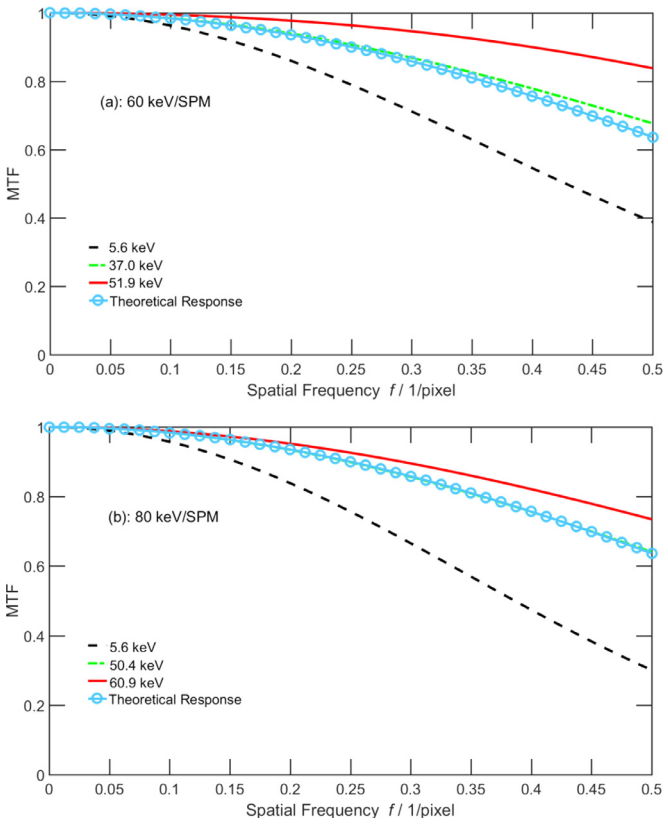

Fig. 2. MTF as a function of the spatial frequency at (a) 60 and (b) 80 keV for single pixel mode (SPM) at various TH0 DAC values. The theoretical response of a detector with square pixels, given by sinc (πf/2) is also shown for comparison.

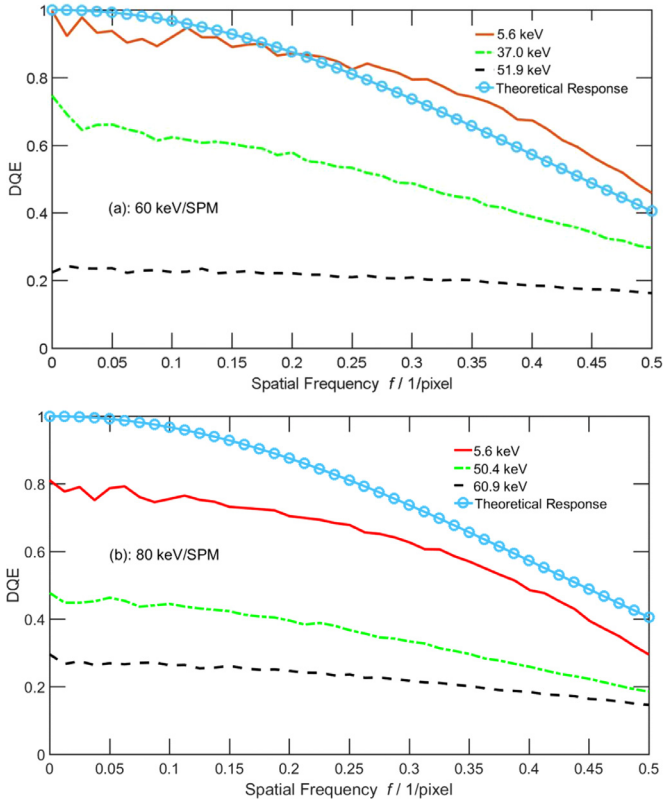

Fig. 3. DQE as a function of the spatial frequency at (a) 60 and (b) 80 keV for Single pixel mode (SPM) at various TH0 DAC values. The theoretical response of a detector with square pixels is also shown for comparison.

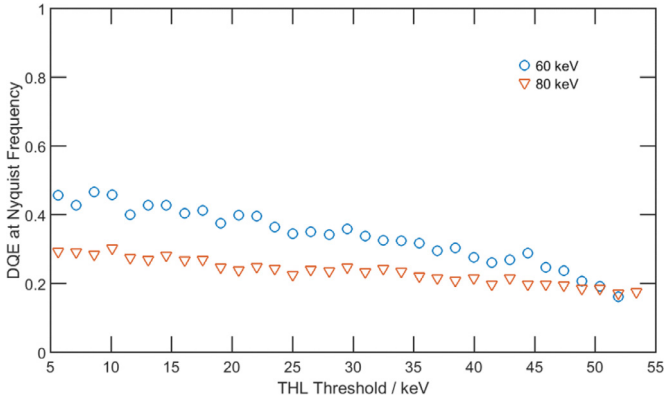

Fig. 4. Variation in DQE at the Nyquist frequency as a function of TH0 threshold values for SPM for 60 and 80 keV primary energies.

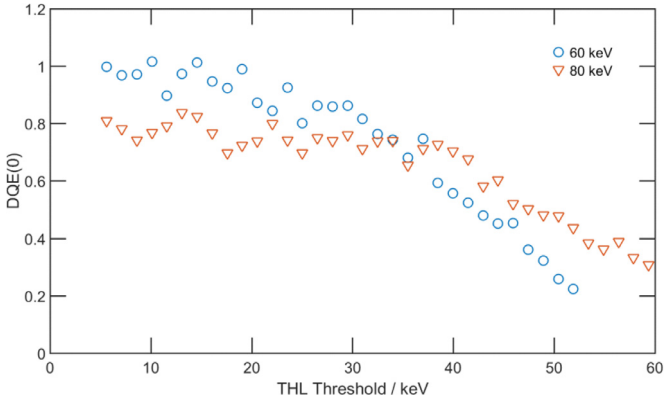

Fig. 5. Variation of DQE(0) as a function of TH0 threshold values for SPM for 60 and 80 keV primary energies.

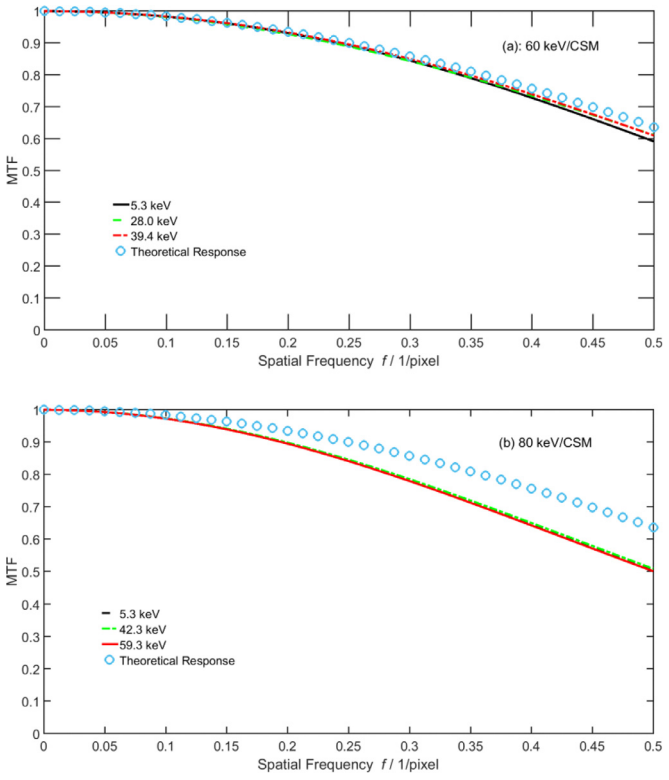

Fig. 6. MTF as a function of spatial frequency at (a) 60 and (b) 80 keV for CSM at various TH0 values. The theoretical response of a detector with square pixels is also shown for comparison.

therefore falls below the threshold for detection. As a result, there is a balance between optimizing the DQE and MTF. The DQE(0) values shown in Figs. 3 and 4 were calculated independently from the analysis of the flat-field images using Eq. (4). Fig. 5 shows the variation of DQE(0) as a function of threshold DAC values.

The degradation of the MTF in Fig. 2(a) and (b) with increasing primary electron energy is consistent with earlier work [9] and with Monte Carlo simulations using the CASINO software package [17] which show that the lateral charge spread (95%) at 60 keV is approximately 25 µm and increases to approximately 42 µm at 80 keV for a 300 µm thick silicon substrate.

At higher energies, long range electron scattering occurs where electrons lose energy over considerable distances from their impact point [17], leading to pixels being triggered far from the initial impact point. The consequent reduction in MTF with increasing electron energy impacts the DQE proportionally (see Eq. (2)) as demonstrated in Figs. 3 and 4 since electron scattering cross sections decrease with increasing primary electron energy. The reduction of DQE with increasing threshold DAC values is similarly attributed to smaller proportion of electrons that exceed the thresholds being detected.

Fig. 5 shows the variation in DQE(0) as a function of TH0 for 60 and 80 keV electrons. It is evident that the slope of the variation of DQE(0) changes when the TH0 threshold is set at half the primary electron energy. Above this point, the NPS is constant since an incoming electron is either recorded in a single pixel or not recorded. Conversely, several pixels may be triggered by a single electron if the threshold is set below this point.

One of the major design advances in the Medipix3 sensor over its predecessors is the implementation of the CSM mode as already described. In principle, CSM should provide excellent MTF performance but without the need to set high values for the energy threshold rejecting electrons that deposit energy across many pixels as required in SPM mode. Thus, in CSM mode using low energy threshold values (with TH0 being the single pixel "arbitrated[1]" threshold and TH1 being the summed charge threshold), almost all detected electrons will be retained, maximising simultaneously the DQE and MTF. Figs. 6 and 7 show the MTF and DQE for the CSM mode. At 60 keV it is clear that the CSM mode gives performance equal to a theoretical square pixel detector with little variation between the three TH1 energy thresholds shown. At 80 keV, the MTF performance is reduced with respect to this theoretical detector values but still maintains high values across the measured spatial frequency range. Fig. 7 shows that these MTF values are matched by high DQE across the spatial frequency range measured. At 60 keV and 80 keV, the DQE values occupy a narrow band, being at most 0.2 and 0.35 lower than the theoretical response of a square pixel detector respectively.

Comparison of the MTF between SPM and CSM modes is shown in Fig. 8 which plots the MTF at the Nyquist frequency as a function of threshold for 60 and 80 keV electrons. It is clear that MTF enhancement is obtained at the lowest energy thresholds using CSM at 60 and 80 keV. In particular, the MTF at the Nyquist frequency value is ca. 0.6 for 60 keV electrons (the theoretical square pixel detector MTF at Nyquist frequency = 0.64) when the energy threshold is set to its lowest value (approximately 5 keV), just above the Medipix3 chip's thermal electronic noise floor. The DQE performance can be compared across the two modes by referring

[1] Single pixel arbitrated means that for a given hit, the counter associated with the threshold TH0 increases if the signal is above TH0 and the signal is the largest in a neighbourhood. This differs from the traditional single pixel mode whereby the counter increases only if the signal is above TH0.

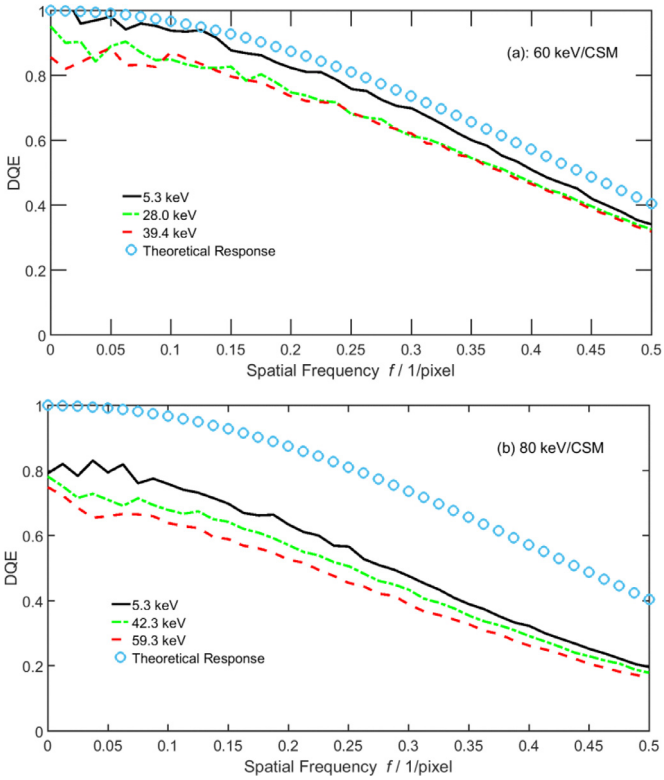

Fig. 7. DQE as a function of the spatial frequency at (a) 60 and (b) 80 keV for CSM at various TH0 values. The theoretical response of a detector with square pixels is also shown for comparison.

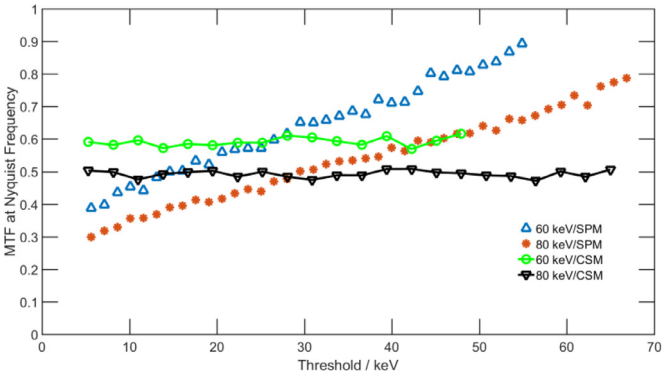

Fig. 8. Comparison of MTF at the Nyquist frequency using SPM and CSM at 60 and 80 keV. TH0 in CSM mode at 60 and 80 keV was set at 4.5 keV for both modes.

to Figs. 3 and 7. In SPM mode, Fig. 3, the DQE exhibits a strong inverse dependence on the TH0 energy threshold where low thresholds yield the highest DQE but lowest MTF (Fig. 8). In CSM mode, Fig. 7, there is no longer a strong dependence on TH0 and the DQE is similar, but slightly lower than that for the lowest SPM energy thresholds (TH0 = 4.5 keV) shown in Fig. 3.

5. Investigation of single electron events

In order to understand the behaviour of the Medipix 3 sensor, the response to single electron events was studied by acquiring flat field images with an exposure time $t = 10\,\mu s$. Fig. 9(a) and (b) show the response of the sensor to single 60 keV electrons when the threshold energy, TH0 is set to 20 keV ($=E_0/3$). Fig. 9(b) shows clearly that portions of the charge generated when single electrons impact the sensor are deposited in neighbouring pixels, creating multi-pixel clusters (in Fig. 9(b) clusters can be seen with areas of 1, 2, 3, and 4 pixels). Increasing the threshold energy TH0 to 40 keV ($=2E_0/3$) (Fig. 9(c) and (d)), shows that only single pixel clusters are obtained but that the overall number of clusters is decreased. This is in consistent with previous measurements by McMullan et al. [8] of the Medipix2 sensor in which for TH0 > $E_0/2$ only single pixel hits are obtained. The variation in the number of clusters counted with respect to threshold energy is plotted in Fig. 9(e) together with the integrated counts obtained from simple summation of all pixel values. Since the average separation of clusters is relatively large for the combination of beam current (105 pA) and shutter time used, the integrated counts can be considered as resulting from the number of clusters counted multiplied by their area in pixels. As such, when TH0 > $E_0/2 = 30$ keV (Fig. 9(e)) the variation in the number of clusters and the integrated counts become equal as only single pixel (unity area) clusters are recorded. Overall, both the number of clusters and integrated intensity decrease (but not monotonically) from a maximum value at TH0 = 4.1 keV to zero at TH0 = E_0 = 60 keV. Similar behaviour is observed for 80 keV electrons (Fig. 9(f)) where a slightly greater number of clusters were counted at TH0 = 4.1 keV due to a higher beam current (120 pA).

The data in Fig. 9(e) and (f) can be decomposed and empirically fitted in order to understand energy deposition and charge sharing in the sensor. Defining the numerical variation in integrated counts with respect to TH0 as $\Sigma(E)$ and the numerical variation in cluster counts with TH0 as $N(E)$, a simple relation can be formed as $C(E) = \Sigma(E) / N(E)$. In Fig. 10(a), the $\Sigma(E)/N(E)$ data is plotted for 60 and 80 keV electrons and depicts the variation of the average area of clusters with respect to TH0. This data is well described by a function: $C(E) = 1 + a\ e^{-E\delta}$ where a and δ are fitted parameters whose values depend on the electron beam energy, E_0. In this analysis we have restricted ourselves to deducing values resulting from least squares fitting although it would also be possible to predict their values based on Monte-Carlo simulations of the detector. Examining the cluster count data further, $N(E)$, in Fig. 10(b), it can be seen that this fits the form:

$$N(E) = N_0\ n(E) = N_0\ erfc\left[\frac{\frac{1}{\sqrt{2}}(E - E_m)}{w}\right] \quad (5)$$

where *erfc* is the complementary error function and N_0, E_m and w are fitted parameters. Therefore the product of the fitted $C(E)$ and $N(E)$ functions shown in Fig. 10(a) and (b) also describes the total detector response, $\Sigma(E)$, as shown in Fig. 10(c).

The function in (5) $N(E) = N_0\ n(E)$ describes a variation in effective pixel area. At TH0 = $E_0/2$, when $C(E) = 1$ pixel, $\Sigma(E)$ equals $N(E)$. However, as the value of TH0 is increased beyond $E_0/2$, the number of pixels registering hits decreases. This is because energies greater than the threshold value can only be transferred if the primary electrons impact pixels in a zone located around the pixel centre with radius less than the pixel half-width. The radius of this zone decreases with increasing TH0 and hence the effective pixel area is continuously reduced. This variation in radius depends on the nature of the energy deposition in the pixels and can be modelled using Monte-Carlo simulations. Calculations were performed using the package CASINO [17] and show that for 60 and 80 keV electrons the average radii for deposition of the full primary electron energy are 11 µm and 20 µm respectively. Thus, in the limit where the threshold energy TH0 = E_0, hits are only detected if the electron strikes the pixel at a maximum distance from its centre defined by difference between the pixel half-width (55 µm/2) and the average radius for full energy deposition. This yields values of 16.5 µm (60 keV) or 7.5 µm (80 keV) radius from the pixel centre. As these radii refer to circular sub-pixel areas the pixels are correspondingly reduced to 8.4% and 1.9% of their full area for 60 and 80 keV electrons respectively.

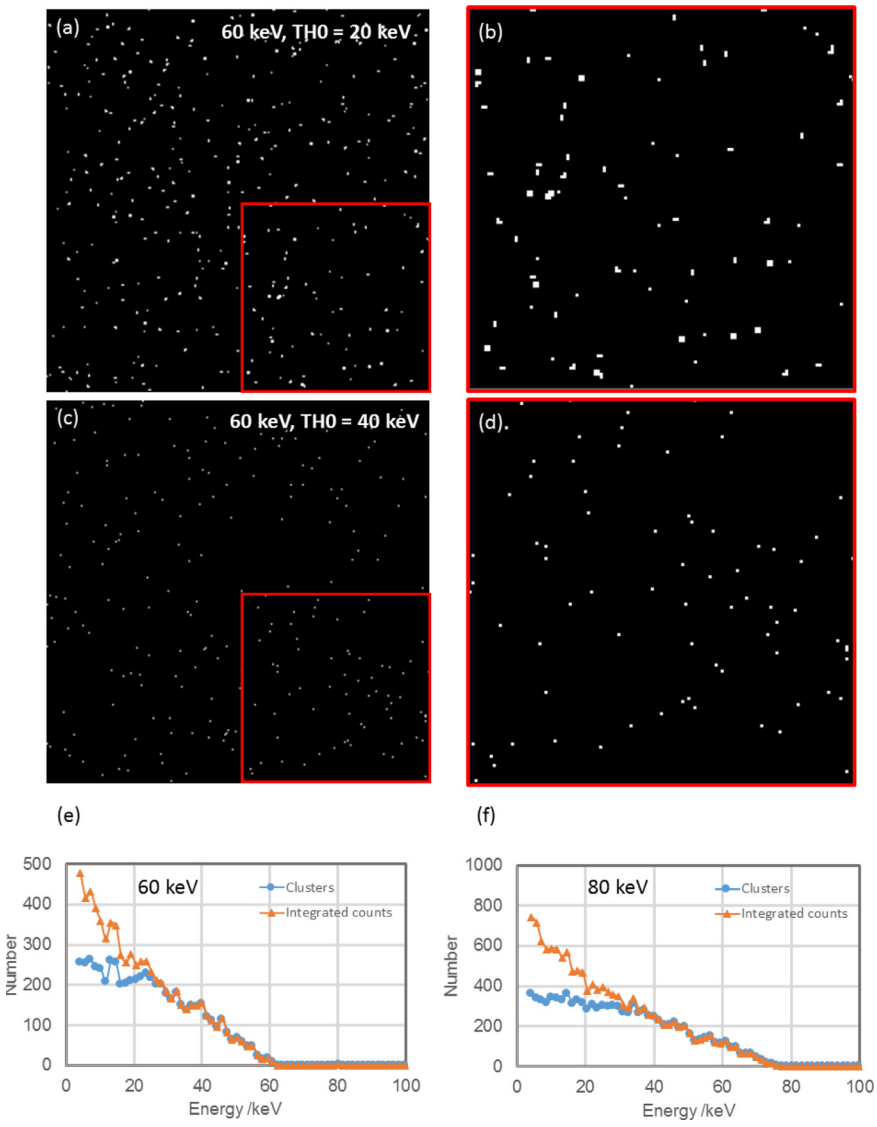

Fig. 9. (a) Single 60 keV electron events with threshold energy, TH0 = 20 keV. (b) Enlarged section taken from (a) showing multi-pixel clusters triggered due to charge spreading. (c) Single 60 keV electron events with TH0 = 40 keV. (d) Enlarged region taken from (c) showing that only single pixels are triggered. (e and f) The variation of integrated image counts and number of clusters counted versus TH0 for 60 keV and 80 keV electrons respectively.

By combining the functions, C(E) and n(E) it is possible to compute the average response of the detector to electrons impacting at a single point to give the PSF. At TH0 values $< E_0/2$, n(E) = 1 and hence C(E) dictates that the average cluster area is greater than 1 pixel. As TH0 approaches $E_0/2$, C(E) tends to 1 and n(E) dictates the overall response, with values <1 that tend to zero at TH0 = E_0. The radii of the clusters are given by $R = \sqrt{C(E)n(E)}/2$ where R plays the role of the variance in an assumed Gaussian PSF. As n(E) takes values in the range 1 to 0 with increasing TH0 value, the radius R is smaller than a single pixel. Therefore, an oversampling factor, M must be used to accurately compute the PSF.

The full expression for the PSF is given by:

$$\mathrm{PSF}(r) = e^{-\frac{1}{\sqrt{2}}\times\left(\frac{r}{RM}\right)^2} \quad (6)$$

where, r is distance from the pixel centre, R, is the cluster radius and M is the oversampling factor. For the PSF computations described an oversampling factor $M = 17$ was found to be sufficient. MTFs were then computed directly from the PSF by a Fourier transform and are shown in Fig. 11(a) and (b) at 60 keV and 80 keV, respectively for a range of TH0 values.

The agreement of the MTF response predicted from single electron event characterization with values obtained from knife edge measurement is assessed in Figs. 12 and 13, in which the MTF values at the Nyquist frequency are plotted as a function of threshold energy. It can be seen that an almost linear variation of the MTF at the Nyquist frequency with respect to threshold energy is obtained from the single electron event analysis and that the gradients are within 1.7X for those measured from the knife edge data. While agreement is not absolute, obtaining similar linear in proximity is supportive of our model for energy deposition in the sensor and also demonstrates prospects for characterization of a counting detector purely by investigating single electron events.

Short, 1 µs exposures, provide insight into the operational performance of the sensor in CSM mode. Fig. 14(a) and (b), show that at 80 keV with TH0 and TH1 set to energy values just above the detector thermal noise floor single electron events are recorded as single pixels. However, this does not necessarily deliver ideal detector performance. Fig. 14(c) shows the integrated intensity from longer, 10 ms exposure, flat field images for both SPM and CSM modes as a function of threshold energy value. For the data recorded in SPM mode, the integrated image intensity decreases

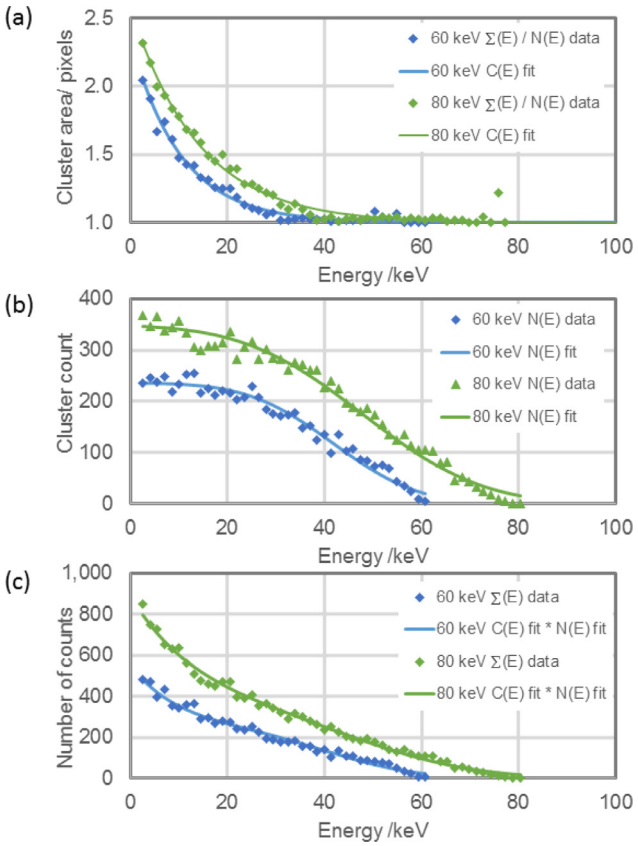

Fig. 10. Analysis of $E_0 = 60$ and 80 keV electron cluster data as a function of threshold energy, TH0. (a) $\Sigma(E)$ data/N(E) data and the fitted cluster area function C(E). (b) N(E) data and fit. (c) $\Sigma(E)$ data and the fit resulting from the product of fits to C(E) and N(E).

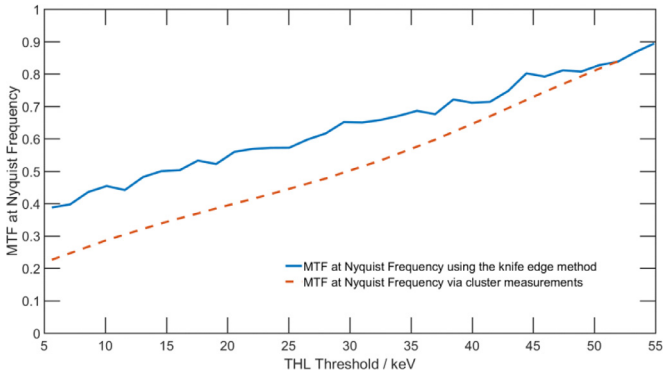

Fig. 12. Comparison of MTFs measured using knife edge method and cluster counting. The plot shows MTF at the Nyquist frequency at 60 keV as a function of TH0 values using SPM mode.

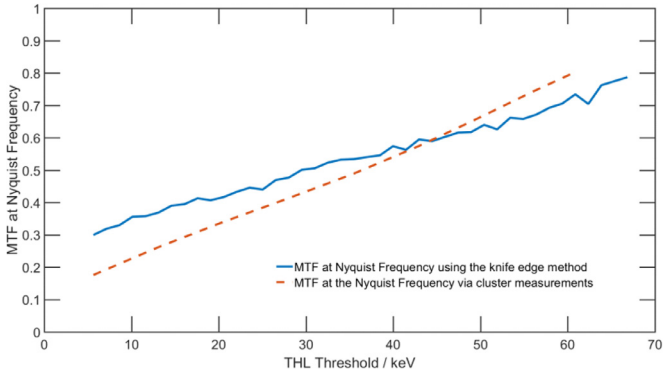

Fig. 13. Comparison of MTFs measured using the knife edge method and cluster counting. The plot shows MTF at the Nyquist frequency at 80 keV as a function of TH0 values in SPM mode.

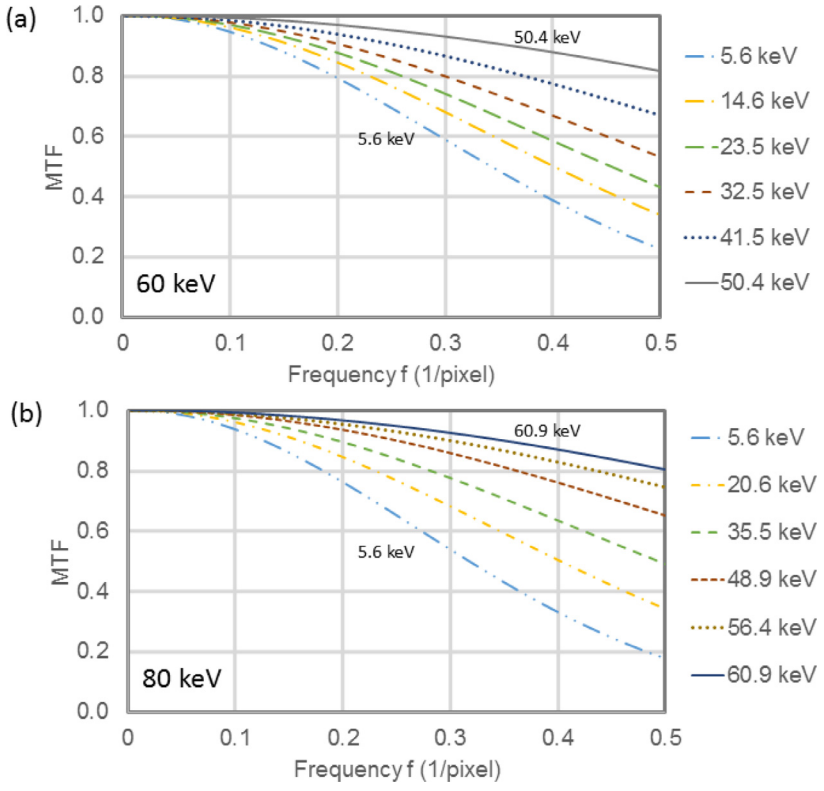

Fig. 11. Calculated MTFs based on synthesized PSFs from single electron event characterisation. (a) 60 keV; (b) 80 keV.

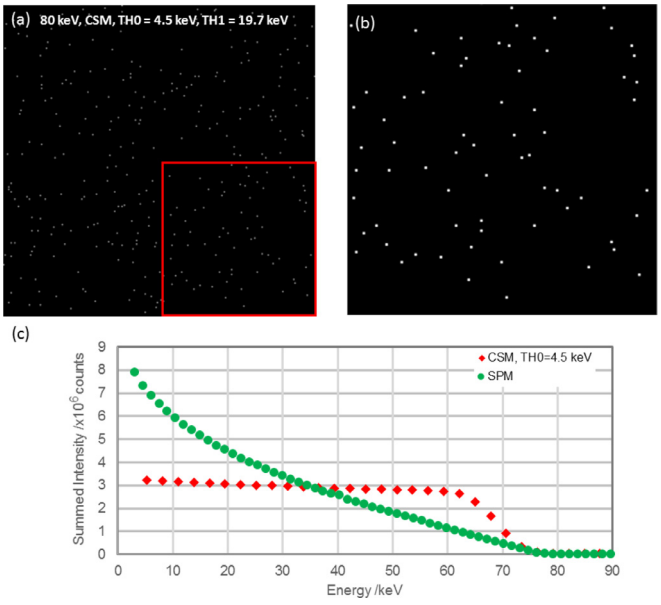

Fig. 14. (a) Single 80 keV electron events captured using CSM mode with TH0 = 4.5 keV and TH1 = 19.7 keV and for an exposure time = 10 µs. (b) Magnified images of the region indicated by the red box in (a) highlighting that electron events are recorded as single pixel events by CSM. (c) Comparison of integrated intensity in flat-field images obtained with exposure time = 10 ms for SPM and CSM modes with respect to energy threshold. (For interpretation of the references to colour in this figure legend, the reader is referred to the web version of this article.).

strongly as a function of threshold energy, from 7.9×10^6 counts at TH0 = 3.0 keV to 0 counts at TH0 = 80 keV (E_0). This is the same response as that obtained by fitting $\Sigma(E) = C(E) \times N(E)$ as in Figs. 9 and 10 for single electron events.

Fig. 14(c) highlights that CSM operation removes much of the variation in integrated intensity, returning an almost constant number of counts for threshold energies from 5 to 60 keV ($3E_0/4$). Closer inspection of the CSM data shown in Fig. 14(c) reveals however, that there is a small linear decrease in counts from 3.22×10^6 at TH1 = 19.7 keV to 2.74×10^6 at TH1 = 59.9 keV. This can be attributed to the CSM algorithm not providing perfect correction for ~15% of electron events at the beam energy used, most likely returning two separated single pixel events. Such events are likely to have been ones in which an incident electron loses significant amounts of energy in pixels separated by two adjacent 2×2 CSM pixel blocks. This could lead to the arbitration circuitry identifying two hits, rather than one. For the CSM mode data at TH1 energy threshold values >60 keV (Fig. 14(c)) it can be seen that the integrated intensity suddenly decreases, reaching zero at 80 keV. The width of the transition relates to the decreasing probability of the CSM algorithm being able to recover all of the deposited charge where at least some charge is deposited in an adjacent 2×2 pixel block.

6. Imaging performance

In this section we demonstrate some new imaging capabilities enabled by the pixel architecture of the Medipix3 sensor. Within the sensor each pixel contains two 12 bit counters which offer operational flexibility for different experimental requirements. For example, it is possible to acquire images with zero gap time between them, enabled by counting into one 12-bit register while simultaneously reading out the other 12-bit register containing counts from the previous image.

It is also possible to configure the two counters as a single 24-bit counter to access a 1 to 16.7×10^6 dynamic range. This capability directly benefits quantitative recording of diffraction patterns including the undiffracted beam. Fig. 15(a) shows a diffraction pattern recorded from Au nanocrystals on a carbon support film (cross-grating replica sample, Agar AGF7016-7) obtained with a parallel beam illuminating many tens of grid squares and with the current reduced by use of a 10 µm condenser aperture to ensure an electron arrival rate <1 MHz in the central spot. Fig. 15(b) shows a typical diffraction pattern recorded in this mode where the number of counts varies from a maximum intensity ca. 10×10^6 counts in the undiffracted beam to a minimum intensity of ca. 3000 counts in reflections at the edge of the pattern.

Fig. 16 shows TEM images that demonstrate, the variation in *MTF* response of the detector according to threshold energy selection and mode (SPM or CSM) as quantified in Figs. 2–6. For a primary microscope magnification of 2MX the cross-grating replica sample was imaged in TEM mode at a beam energy of 60 keV. In Fig. 16(a), in SPM mode with TH0 = 20 keV, exposure time = 500 ms, Au crystals are observed on the amorphous carbon support. Fig. 16(b) shows the power spectrum for the region enclosed by the solid red box. In Fig. 16(c), the effect of changing the threshold energy to $>E_0/2$, TH0 = 40 keV, highlights the improvement in the MTF, with both lattice fringes and Moiré contrast recorded in the Au nanocrystals (examples being highlighted by the white dashed boxes in Figs. 16(c) compared to none being visible for the same regions in Fig. 16(a)). The power spectrum in Fig. 16(d), for the region enclosed by the red box, now shows an intensity peak, corresponding to lattice fringes, at a radius very close to the Nyquist frequency. The scale bars in the images have been set, assuming the observed fringes to be {111} planes with a physical spacing of 0.235 nm. Selection of a higher threshold energy (Fig. 16(c)), resulted in 2.1X lower counts and so an increased exposure time of 1000 ms was used to maintain the signal to noise ratio. Fig. 16(e) shows that by operating in CSM mode, where both TH0 and TH1 were set to values just above the detector thermal noise floor, {111} type lattice fringes were visible in a single area of an image recorded with a 500 ms exposure time and with mean counts similar to those in Fig. 16(a). Power spectrum analysis, in Fig. 16(f), performed for the region enclosed by the red box in Fig. 16(e), provides evidence for the observation of lattice fringes, albeit with weaker contrast than in Fig. 16(c). Overall, Fig. 16(e) demonstrates a simultaneous high DQE and MTF as predicted from the data in Figs. 6–8.

7. Conclusions

We have performed a comprehensive analysis of the imaging response of the Medipix3 sensor at 60 keV and 80 keV electron beam energies. Our measurements of the MTF and DQE in single pixel mode using conventional knife edge and flat field image methods agree with trends already observed for the Medipix2 detector [8]. We have also reported data using the SPM mode by analysing single electron events and producing an empirical model that can be used to directly predict the MTF response of the detector. This empirical model yields data that closely agrees with the data from the accepted knife edge method measurements and also provides insight into the variation of the integrated intensity at low threshold energies due to the area the clusters generated and at high thresholds due to the reduction in the effective pixel size. The latter phenomenon is responsible for obtaining MTF values which exceed the theoretical response of a square pixelated detector, but at the expense of a substantially reduced DQE. Prediction of the MTF from single electron events has been reported previously [18] however, our method, differs in that it synthesises a PSF based on empirical fitting of the integrated intensity and sin-

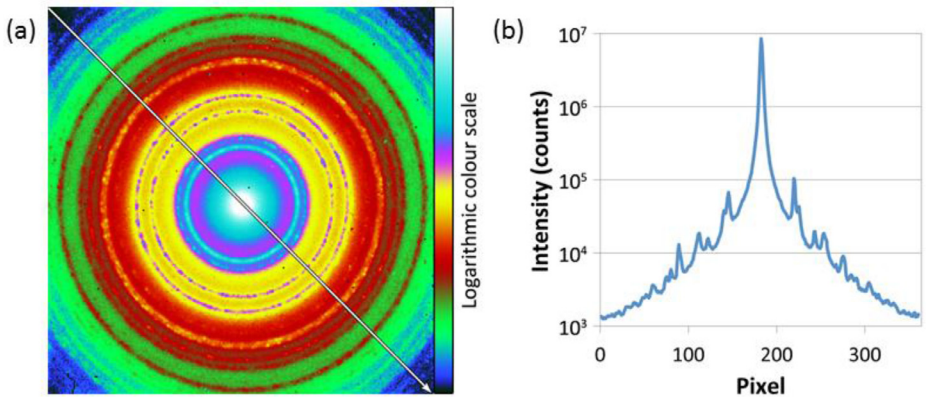

Fig. 15. 24-bit depth acquisition of a diffraction pattern. (a) Diffraction pattern shown on a logarithmic colour scale to highlight features across the full intensity range. (b) Singe-line profile along the pattern diagonal as indicated showing the dynamic range of the information contained in the pattern.

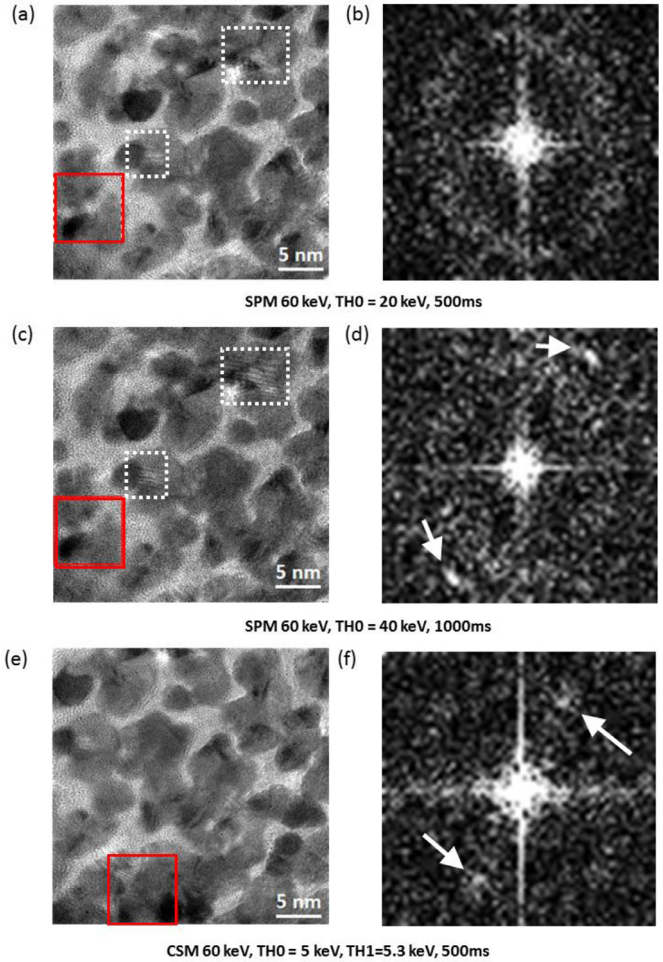

Fig. 16. Images of Au nano-crystals in a cross-grating replica sample acquired at 60 keV. (a) SPM mode with TH0 = 20 keV, exposure time = 500 ms, (b) power spectrum for red boxed region of (a), (c) SPM mode with TH0 = 40 keV, exposure time = 1000 ms. (d) Power spectrum for red boxed region of (c). (e) CSM mode with TH0 = 5.0 keV, TH1 = 5.3 keV and exposure time = 500 ms. (f) Image power spectrum for red boxed region of (e). White dashed boxes in (a) and (c) indicate identical sample regions and highlight the absence/presence of lattice/Moiré fringes obtained by changing the SPM mode TH0 energy threshold. (For interpretation of the references to colour in this figure legend, the reader is referred to the web version of this article.).

gle event counting. It is also easier to implement across datasets where images are acquired as a function of detector threshold energy.

We have demonstrated that the charge summing mode (CSM) implemented the Medipix3 sensor results in significant and simultaneous improvements in the MTF and DQE at both electron beam energies considered. However, due to the mechanism of energy loss in the sensor material, we have shown that the CSM algorithm does not provide perfect identification of all single electron events or recovery of all spatially distributed charge. These factors most likely explain why the CSM MTF and DQE responses are excellent but below that of a theoretical square pixel detector. Thus, it is clear that the CSM mode should have obvious applications for efficient low dose imaging of electron beam sensitive materials.

Primary electron energies of 60–80 keV are highly relevant in the imaging of 2D materials such as graphene [7,19]. However, primary energies between 160–300 keV are more commonly used in many materials science applications of radiation resistant materials as they enable higher spatial resolution [19]. These beam energies lead to large average lateral dispersion (for 200 keV ~190 μm, i.e. larger than two pixels range) in a silicon sensor material [17]. In a future study we will investigate both SPM and CSM operation modes at high electron flux in order to understand the extent to which the CSM algorithm can provide performance improvements and the nature of how it will fail in this regime.

Acknowledgements

We gratefully acknowledge the contributions of Dr S. McFadzean and Mr D. Doak who provided expert technical assistance and fabrication of the detector housing.

This work was partly supported by EPSRC grant EP/M009963/1 (Fast Pixel Detectors: a paradigm shift in STEM imaging). Financial support from the European Union under the Seventh Framework Program under a contract for an Integrated Infrastructure Initiative (Ref 312483-ESTEEM2) is gratefully acknowledged.

References

[1] G. McMullan, A.R. Faruqi, R. Henderson, N. Guerrini, R. Turchetta, A. Jacobs, G. van Hoften, Experimental observation of the improvement in MTF from backthinning a CMOS direct electron detector, Ultramicroscopy 109 (2009) 401–1147.

[2] R. Ballabriga, M. Campbell, E. Heijne, X. Llopart, L. Tlustos, W. Wong, Medipix3: a 64 k pixel detector readout chip working in single photon counting mode with improved spectrometric performance, Nucl. Instrum. Methods Phys. Res. A 633 (May 2011) S15–S18 Supplement 1ISSN 0168-9002.

[3] M.W. Tate, P. Purohit, D. Chamberlain, K.X. Nguyen, R. Hovden, C.S. Chang, P. Deb, E. Turgut, J.T. Heron, D.G. Schlom, D.C. Ralph, G.D. Fuchs, K.S. Shanks, H.T. Philipp, D.A Muller, SM Gruner, High dynamic range pixel array detector for scanning transmission electron microscopy, Microsc. Micronal 1 (2016) 237–249.
[4] G. McMullan, A.R. Faruqi, R. Henderson, Direct electron detectors, Methods Enzymol. 579 (2016) 1–17.
[5] J. Park, H. Elmlund, P. Ercius, J.M. Yuk, D.T. Limmer, Q. Chen, K. Kim, S.H. Han, D.A. Weitz, A. Zettl, A.P. Alivisatos, 3D structure of individual nanocrystals in solution by electron microscopy, Science 349 (2015) 290–295.
[6] E. Majorovits, I. Angert, U. Kaiser, R.R. Schroder, Benefits and limitations of low-kV macromolecular imaging of frozen hydrated biological samples, Biophys. J. 110 (2016) 776–784.
[7] A.W. Robertson, C.S. Allen, Y.A. Wu, K. He, J. Olivier, J. Neethling, A.I. Kirkland, J.H. Warner, Spatial control of defect creation in graphene at the nanoscale, Nat. Commun. 3 (2012) 1144.
[8] G. McMullan, D.M. Cattermole, S. Chen, R. Henderson, X. Llopart, C. Summerfield, L. Tlustos, A.R. Faruqi, Electron imaging with Medipix2 hybrid pixel detector, Ultramicroscopy 107 (2007) 401–413.
[9] G. McMullan, et al., Detective quantum efficiency of electron area detectors in electron microscopy, Ultramicroscopy 109 (2009) 1126–1143.
[10] R. Ballabriga, The design and implementation in 0.13 µm CMOS of an Algorithm permitting spectroscopic imaging with high spatial resolution for hybrid pixel detectors Ph.D. thesis, Universitat Ramon Llull, 2009.
[11] D. Pennicard, R. Ballabriga, X. Llopart, M. Campbell, H. Graafsma, Simulations of charge summing and threshold dispersion effects in medipix3, Nucl. Instrum. Methods Phys. Res. A 636 (2011) 74–81.
[12] R.R. Meyer, A.I. Kirkland, R.E. Dunin-Borkowski, J.L. Hutchison, Experimental characterisation of CCD cameras for HREM at 300 kV, Ultramicroscopy 85 (1) (2000) 9–13.
[13] R.R. Meyer, A.I. Kirkland, The effects of electron and photon scattering on signal and noise transfer properties of scintillators in CCD cameras used for electron detection, Ultramicroscopy 75 (1998) 23.
[14] S. McVitie, D. McGrouther, S. McFadzean, D.A. MacLaren, K.J. O'Shea, M.J. Benitez, Aberration corrected Lorentz scanning transmission electron microscopy, Ultramicroscopy 152 (2015) 57.
[15] R. Plackett, I. Horsewell, E.N. Gimenez, J. Marchal, D. Omar, N. Tartoni, Merlin: a fast versatile readout system for Medipix3, J. Instrum. 8 (2013) Article number C01038.
[16] R.S. Ruskin, Z. Yu, N. Grigorieff, Quantitative characterization of electron detectors for transmission electron microscopy, J. Struct. Biol. 184 (2013) 385–393.
[17] D. Drouin, A.L. Couture, D. Joly, T. Xavier, A. Vincent, G. Raynland, CASINO V2.42-a fast and easy-to-use modelling tool for scanning electron microscopy and microanalysis users, Scanning 29 (3) (2007) 92–101.
[18] R Ghadimi, I Daberkow, C Kofler, P Sparlinek, H Tietz, Characterization of 16 MegaPixel CMOS detector for TEM by evaluating single events of primary electrons, Microsc. Microanal. 17 (2011) 1208–1209 Suppl. 2.
[19] H.H. Rose, Historical aspects of aberration correction, J. Electron Microsc. 58 (2009) 77–85.